Simulations of Incompressible Separated Turbulent Flows around Two-Dimensional Bodies with URANS Models in OpenFOAM

Andrew B. Porteous[1], Robert D. Habbit, III [2], Juan D. Colmenares Fernandez[3], Svetlana V. Poroseva[4]
The University of New Mexico, Albuquerque, New Mexico, 87131

Scott M. Murman[5]
NASA Ames Research Center, Moffett Field, CA 94035

The goal of this study is to determine whether an unsteady formulation of a RANS turbulence model leads to improved description of incompressible separated turbulent flows around two-dimensional bodies. Two geometries are considered: a NACA 4412 airfoil and a circular cylinder. Simulations are conducted with two-equation turbulent models: Menter's 1994 Shear Stress Transport model and Wilcox's 2006 k-ω model, implemented in the open-source CFD OpenFOAM software. Comparison with experimental data and computational results obtained from Large and Detached Eddy Simulations as well as with URANS/RANS models by other research groups is also provided.

Nomenclature

Re = *Reynolds number,* $U_\infty \rho / \nu$
M = *Mach number,* U_∞ / a
ρ = *density*
P = *pressure*
a = *speed of sound*
U_∞ = *free stream velocity*
u = *streamwise velocity component*
v = *vertical velocity component*
u' = *velocity fluctuation in the streamwise direction*
I = *turbulence intensity,* u'/U_∞
ν = *kinematic viscosity*
μ = *dynamic viscosity*
c = *chord*
C_p = *pressure coefficient,* $(P - P_\infty)/0.5\rho U_\infty^2$
C_{pb} = *base pressure coefficient at* $\theta = 180°$
C_D = *drag coefficient,* $F_D/0.5\rho U_\infty^2\, A$
C_L = *lift coefficient,* $F_L/0.5\rho U_\infty^2\, A$
C_f = *friction coefficient,* $\tau_w/0.5\rho U_\infty^2$
A = *frontal area*
F_D = *drag force*

---

[1] Graduate Student, Mechanical Engineering, MSC01 1105, 1 UNM Albuquerque, NM, 87131-00011, AIAA Student Member.

[2] Graduate Student, Mechanical Engineering, MSC01 1105, 1 UNM Albuquerque, NM, 87131-00011, AIAA Student Member.

[3] Graduate Student, Mechanical Engineering, MSC01 1105, 1 UNM Albuquerque, NM, 87131-00011, AIAA Student Member.

[4] Assistant Professor, Mechanical Engineering, MSC01 1104, 1 UNM Albuquerque, NM, 87131-00011, AIAA Associate Fellow.

[5] Aerospace Engineer, NASA Ames Research Center, Moffett Field, CA, 94035.

F_L = *lift force*
D = *diameter*
τ_w = *wall shear stress*
u_τ = *friction velocity*, $\sqrt{\tau_w/\rho}$
x = *streamwise flow direction*
y = *normal-to-wall direction*
y^+ = *dimensionless distance from the wall based on fluid properties*, yu_τ/ν
y_w = *distance between a wall and the first grid node in the y-direction*
t = *time*
$t*$ = *dimensionless time* $\Delta tU_\infty/D$
θ = *azimuth angle measured clockwise from the stagnation point*
ϕ = *separation angle measured clockwise from the stagnation point*
α = *angle of attack*
ω = *turbulent specific dissipation*, ε/k
ε = *turbulent scalar dissipation*
k = *turbulent kinetic energy*
β_1 = *blending constant*, $\beta_1 = 0.075$
L_R = *recirculation length*
h = *characteristic mesh length for the constant domain size*, $1/\sqrt{N}$
N = *total number of nodes in the computational domain*

I. Introduction

IN the current study, results of simulations conducted with Reynolds-Averaged Navier-Stokes (RANS) and Unsteady RANS (URANS) turbulence models in incompressible turbulent flows around two-dimensional (2D) bodies are presented. The NACA 4412 airfoil and a circular cylinder are chosen to represent streamlined and bluff bodies, respectively. Both flows have areas of flow separation that are not well predicted with RANS models.[1-5] The purpose of this study is to analyze whether an unsteady formulation of a RANS turbulence model improves model's prediction of the size and location of separation zones in such flows.

Turbulence models used in the simulations are two-equation models: Menter's 1994 Shear Stress Transport (SST) model[6] and Wilcox's 2006 k-ω model[7] in their standard formulation.[8] Simulations are conducted with the open-source computational fluid dynamics (CFD) solver OpenFOAM.[9] Previously, it was demonstrated that results obtained with these two models implemented in OpenFOAM are of comparable accuracy with those obtained with the high-fidelity NASA CFL3D and FUN3D codes[8] in a few benchmark turbulent flows including a flow around the NACA 4412 airfoil.[10,11] Only the results of steady-state flow simulations were discussed in Refs. 10 and 11.

In the paper, results of URANS simulations are compared with available experimental and computational data. For a flow around a circular cylinder, comparison is made with experimental data from Refs. 12-17 and Large Eddy Simulation (LES), Detached Eddy Simulations (DES), URANS and RANS data from Refs. 18-22. Experimental[23-25] and RANS[8] data are used to compare the NACA 4412 airfoil flow results with .

II. Computational Methods

Equations solved for the SST and k-ω models[6,7] in the current study are the same as given in Ref. 8 and previously implemented in OpenFOAM[10] (corresponding corrections to the original OpenFOAM solver can be downloaded from Dr. Poroseva's website[26] at the University of New Mexico). The Semi-Implicit Method for Pressure-Linked Equations (SIMPLE) algorithm is used in steady-flow simulations. The SIMPLE algorithm solves iteratively for the velocity and pressure fields from predefined initial conditions in incompressible steady-state flow simulations. The discretization scheme applied is the second-order Gaussian integration scheme. The interpolation schemes are the first order linear approximations, except for the divergence scheme which uses upwind approximations. For the Laplacian scheme, the surface normal gradient scheme is chosen, which is a corrected unbounded, second order, conservative scheme[9].

In the unsteady flow simulations, the Pressure Implicit with Splitting Operators (PISO) algorithm is used. The PISO algorithm solves for pressure and velocity fields using predefined initial conditions in transient turbulent incompressible flow simulations. For time discretization, a backward second-order implicit scheme is implemented. The interpolation, gradient, and Laplacian schemes are the same as those used with the SIMPLE algorithm.

III. Computational Domain

A. Grids

The computational domains used in simulations for the two flows are shown in Figs. 1 and 2. The structured C-type mesh for the NACA 4412, 897×257 with 513 points along the airfoil surface, was generated at NASA and is available at the Turbulence Model Benchmarking Working Group's website.[8] The far field boundaries of the computational domain are a hundred times the cord length away. The computational node next to the wall is at y^+ between 0.2 and 0.4.

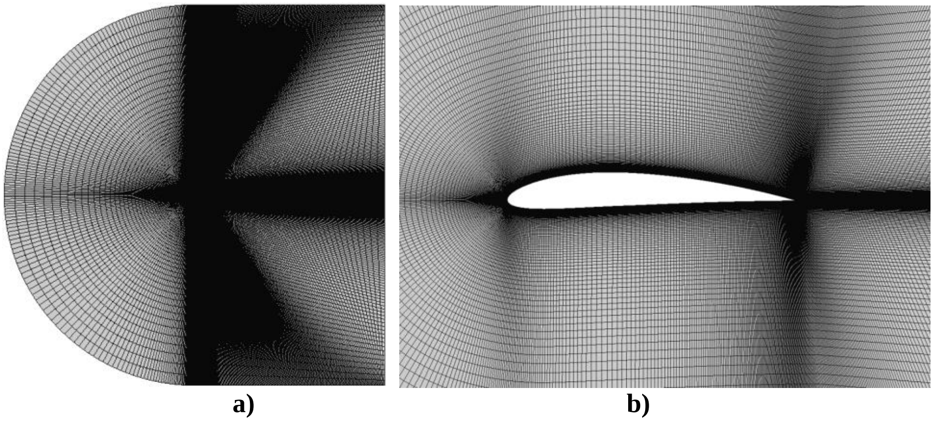
a) b)

Figure 1. Grid 897×257 (513 Points on Airfoil Surface): a) complete computational domain, b) zoomed view of the grid near the airfoil surface.

In simulations of a flow around a circular cylinder, a hybrid O/C-type mesh is used (Fig. 2). The cylinder diameter D is 1 m. Its center is located at the grid origin. The grid transition from the O- to C-type occurs at a distance of four diameters from the grid origin. Upstream and downstream boundaries are located 100D from the origin. The hybrid O/C-type computational mesh was used to reduce the total number of cells in the far field while utilizing the appropriate refinement near the cylinder wall and in its wake. Four grids with the increasing refinement are used in this study. At the maximum Reynolds number considered for this geometry, $Re = 3.6 \times 10^6$, the y^+ values are less than 2 for the coarsest grid, G1, and less than 0.65 for the finest grid, G4. Table 1 compares the number of elements and the number of nodes used in the four grids.

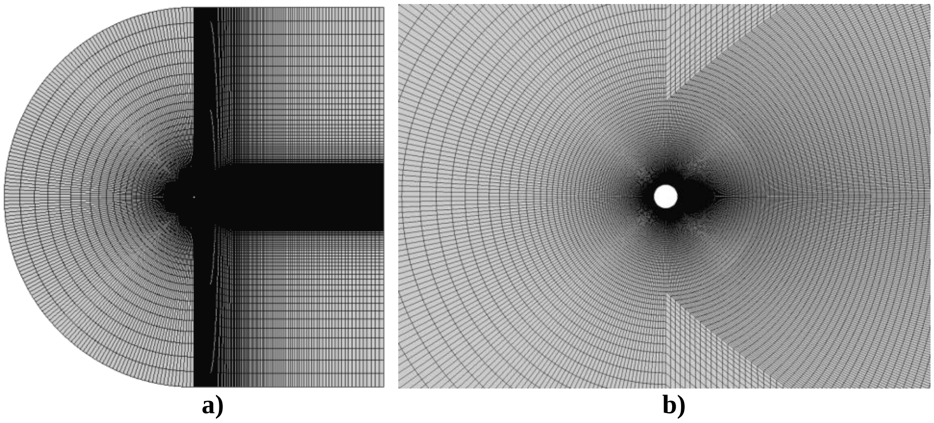
a) b)

Figure 2. Computational domain and grid (G3) for the circular cylinder simulations: a) complete computational domain b) zoomed view of the grid near the cylinder surface.

Table 1. Details of the grids used in the circular cylinder simulations.

Grid	Number of elements	Total number of nodes	Nodes on the cylinder surface	O-Grid: nodes in the radial direction (0.5D ≤ x ≤ 4D)	C-Grid: number of nodes at the grid symmetry axis	
					-100D ≤ x ≤ -4D	4D ≤ x ≤100D
G1	14310	29004	132	65	15	45
G2	57240	115248	264	130	30	90
G3	128790	258732	396	195	45	135
G4	228960	459456	448	260	60	180

B. Boundary and Initial Conditions

The flow parameters used in simulations of a flow around the NACA 4412 airfoil are set to match the experimental data.[23-25] The inlet boundary conditions are located at the left side of the computational domain (Fig. 1), with the prescribed inlet velocity corresponding to M = 0.09 and viscosity defined from simulations at the Reynolds number based on the chord length of Re = 1.52×10^6. The zero gauge pressure outlet condition is applied to the far field boundary condition on the right side of the computational domain. This is also the initial condition for the internal pressure field. The no-slip boundary condition is applied on the airfoil surface.

Initial conditions for the turbulent kinetic energy, k, and the specific dissipation rate, ω, are as in Ref. 8:

$$k_{farfield} = \frac{3}{2}(U_\infty I)^2, \qquad \omega_{wall} = 10\frac{6\nu}{\beta_1 {y_w}^2}\,, \qquad \omega_{farfield} = 1\times10^{-6}\frac{\rho_\infty a_\infty^2}{\mu_\infty}. \tag{1}$$

The flow conditions in simulations of a flow around a circular cylinder match those used in the experiments.[12-17] The inlet is located on the left side of the computational domain with a free stream velocity, U_∞, based on the Mach number M = 0.04 and a turbulence intensity of $I = 0.007$. Viscosity is based on the Reynolds number used in simulations: $Re = 10^6$, 2×10^6, 3×10^6, and 3.6×10^6. The outlet condition is located on the right side of the computational domain and is set to have a zero gage pressure. The initial internal velocity and pressure fields are the same as at the inlet and outlet, respectively. The initial condition for the turbulent kinetic energy and specific dissipation rate are obtained from Eq. (1).

Flow parameters used in unsteady flow simulations are the same as in the steady-state flow calculations. In flow simulations around a cylinder, the time step, $\Delta t U_\infty/D = 0.005$, is used as recommended in Ref. 27, which also corresponds to a half of that in Ref. 18. In airfoil flow simulations, a smaller time step was used to avoid computational instabilities. However, neither with the time step corresponding to the Courant-Friedrichs-Lewy condition equal to one, nor with the time step reduced by an order of magnitude to 1×10^{-6} seconds, an unsteady flow around the NACA 4412 airfoil was not detected with the two turbulence models implemented in OpenFOAM. All attempted URANS solutions converged to the steady-state solution for the given flow parameters.

IV. Results

A. NACA 4412 Airfoil

The results of simulations of an incompressible turbulent flow around the NACA 4412 airfoil using standard steady-flow formulations of two-equation RANS turbulence models implemented in OpenFOAM were previously presented in Ref. 10. It was found that Menter's SST model produces more accurate results than the k-ω model in this flow geometry. Slight disagreement observed in Ref. 10 between the SST model results and those obtained with the NASA FUN3D and CFL3D solvers[8] was found to be due to a typo in the SST model implementation, which was corrected before conducting unsteady-flow simulations. Corrected SST model profiles of the streamwise and transverse velocity components obtained on the 897×257 grid at the angle of attack $\alpha=13.87^o$ are shown by solid lines in Figs. 3 and 4, respectively. Computational profiles in Fig. 3 are received along the line probes extended normally from the airfoil surface at locations where experimental[23,24] and CFL3D and FUN3D data[8] are available. In the figures, symbols correspond to experimental data and the dashed lines are from Ref. 8. The results obtained are in close agreement with the CFL3D and FUN3D data. A good agreement with the experimental data is observed for the streamwise velocity component (Fig. 3a). However, predictions of the traverse velocity component in the separation zone are less adequate (Fig. 3b). Figure 4b represents the flow field for velocity magnitude at $\alpha=13.87^o$. This contour plot shows how small the separation bubble is in comparison to the chord length.

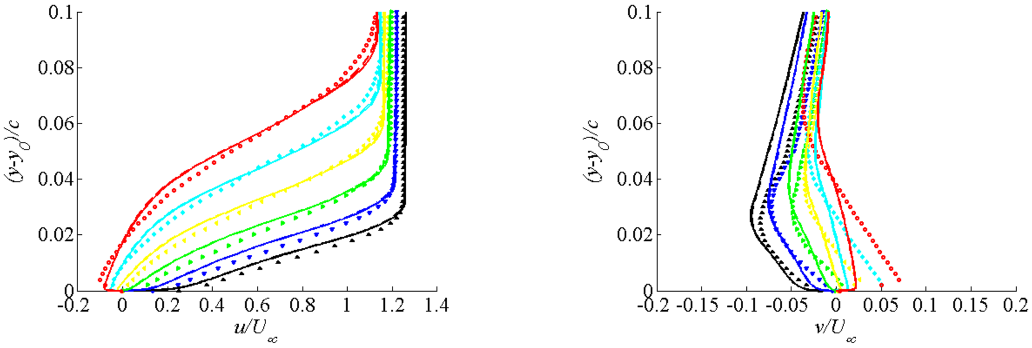

a) b)

Figure 3. Menter's SST model[6] profiles of the a) streamwise and b) transverse velocity components in a flow around the NACA 4412 airfoil on the grid 897×257. Notations: experimental data[23,24] ▲ x/c=0.6753, ▼ x/c=0.7308, ▶ x/c=0.7863, ◀ x/c=0.8418, ♦ x/c=0.8973, ● x/c=0.9528; computational profiles: - - - FUN3D and CFL3D[8], —— OpenFOAM.

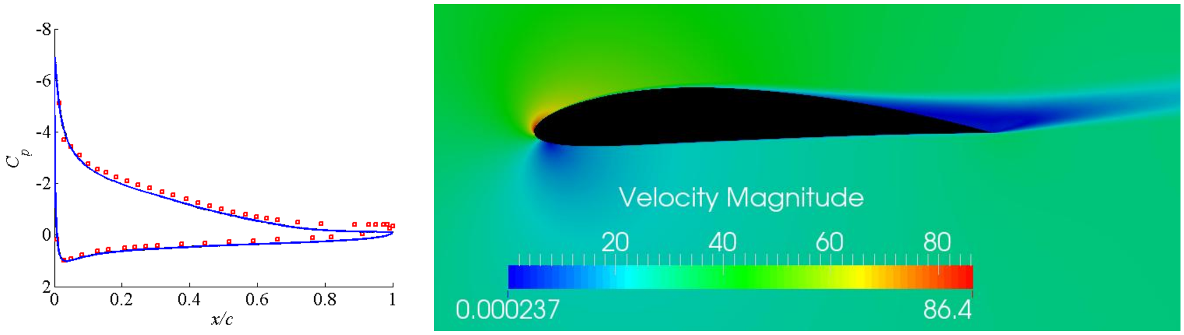

a) b)

Figure 4. A flow around the NACA 4412 airfoil on the grid 897×257 with Menter's SST model[6] a) pressure coefficient b) contour plot of the velocity magnitude at α=13.87° with $U_\infty = 36.67\, m/s$. Notations: □ experimental data[23,24], - - - FUN3D and CFL3D[8], —— OpenFOAM.

In addition to previous computations[10], steady-state flow simulations were conducted for the NACA 4412 airfoil at different angles of attack. Figure 5 shows variations of the lift coefficient against the angle of attack obtained with the two turbulence models. Menter's SST model underpredicts the lift coefficient, with the tendency increasing with the growth of the angle of attack. Simulations at the angle of attack higher than the stall angle failed. The *k-ω* model[7] overpredicts both the lift coefficient and the stall angle.

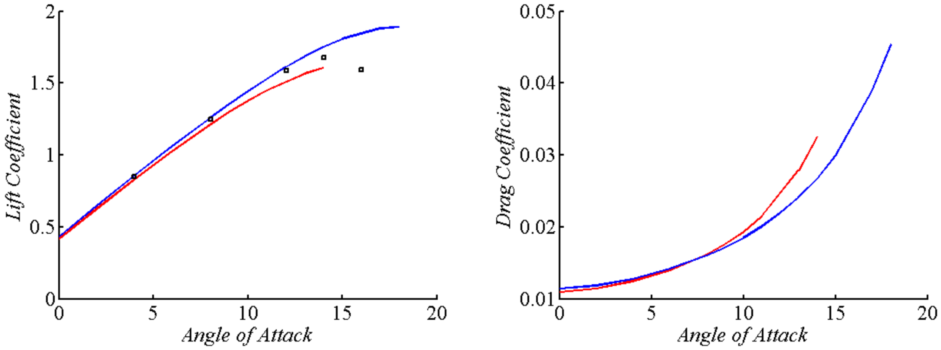

a) b)

Figure 5. a) Lift and b) Drag coefficients vs. the angle of attack. Notations:□ experimental data[23,24] —— experimental data[23,24] at $Re = 1.52\times10^6$, simulations —— *k-ω*, —— Menter SST.

Unsteady simulations conducted with the two models tend to convert to steady-state flow solution in this geometry regardless of the different time steps and the accuracy order of time-discretization schemes used. In some cases, oscillating solutions were observed, but determined to be of an unphysical nature.

B. Circular Cylinder

Table 2. Grid sensitivity study at $Re = 3.6 \times 10^6$.

Turbulence model/method	C_D	St	ϕ	L_r/D	$-C_{pb}$
G1 RANS k-ω	0.4567	~	117.6°	0.82	0.271
G2 RANS k-ω	0.3527	~	115.5°	1.08	0.299
G3 RANS k-ω	0.3197	~	114.4°	1.26	0.308
G4 RANS k-ω	0.3029	~	113.8°	1.37	0.308
G1 URANS k-ω	0.5012	0.196	120.8°	0.31	0.737
G2 URANS k-ω	0.5075	0.187	122.8°	0.19	0.672
G3 URANS k-ω	0.4369	0.180	120.3°	0.34	0.551
G4 URANS k-ω	0.4107	0.171	118.9°	0.42	0.513
G1 RANS SST	0.5411	~	110°	1.02	0.373
G2 RANS SST	0.4605	~	107.6°	1.29	0.411
G3 RANS SST	0.4335	~	106.9°	1.41	0.411
G4 RANS SST	0.4181	~	106.6°	1.49	0.411
G1 URANS SST	0.5524	0.178	112°	0.49	0.681
G2 URANS SST	0.5736	0.167	115°	0.33	0.719
G3 URANS SST	0.4392	0.157	108.8°	0.99	0.532
G4 URANS SST	0.4206	0.148	107.8°	1.23	0.495

A grid sensitivity study for a flow around a smooth circular cylinder was performed at the Reynolds number of $Re = 3.6 \times 10^6$. Steady and unsteady-flow simulations were conducted with the same formulations of SST and k-ω turbulence models as described in the previous sections. Results for unsteady simulations are time averaged for a dimensionless time $\Delta t U_\infty / D = 300$ in the stage of converged oscillations. The coefficient of drag is the last value to converge in unsteady simulations. Therefore, the solution is considered to be converged when the coefficient of drag is oscillating between constant maximum and minimum values (Fig. 6). Four different grids with the parameters given in Table 1 are used in this study. The effect of the grid resolution on the drag coefficient, C_D, separation angle, ϕ, and recirculation length, L_r/D, as well as the base pressure coefficient, C_{pb}, is shown in Table 2.

Figure 7 further illustrates variations of the base pressure coefficient, C_{pb}, (pressure coefficient at $\theta = 180°$) and the separation angle, ϕ, with the characteristic mesh length, $h = 1/\sqrt{N}$. As one can see, the tendency for solutions to converge is observed, but not all flow parameters have reached their limit values. The limit values seem to vary for different turbulence models and for steady and unsteady formulations of the same model. In particular, the difference in the drag coefficient values obtained with G3 and G4 meshes is ~5.4% for RANS k-ω, 6.2% for URANS k-ω, 3.6% for RANS SST, and 4.3% for URANS SST models. Due to time limitations, simulations with more refined grids were not conducted. Results presented below are from simulations conducted with the G4 grid.

Flow simulations were conducted at four Reynolds numbers: $Re = 10^6,\ 2 \times 10^6,\ 3 \times 10^6,$ and 3.6×10^6 to compare with available experimental and computational results. These Reynolds numbers are considered to be in the supercritical flow regime, where the boundary layer is completely turbulent prior to separation.[18] Data of wind tunnel experiments (Achenbach,[12] Roshko,[13] Schewe,[14] Jones et al.,[15] Schmidt,[16] and Shih[17]) are used along with three-dimensional (3D) LES and RANS/URANS data from Catalano et al.[18]. 2D URANS data is also available from Karabelas et al.[19] and Ong et al.[20], 3D DES data from Travin et al.[21] and Lo et al.[22]. RANS/URANS simulations in Refs. 18-20 were conducted with the k-ε turbulence model in different formulations.

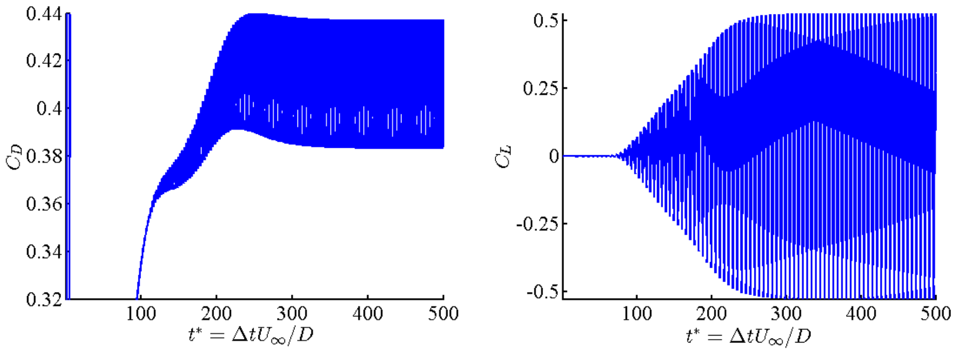

a) b)

Figure 6. Transient loads with respect to $t^* = \Delta t U_\infty / D$ on the G4 mesh with the k-ω turbulence model at $Re = 3.6 \times 10^6$. a) drag coefficient b) lift coefficient.

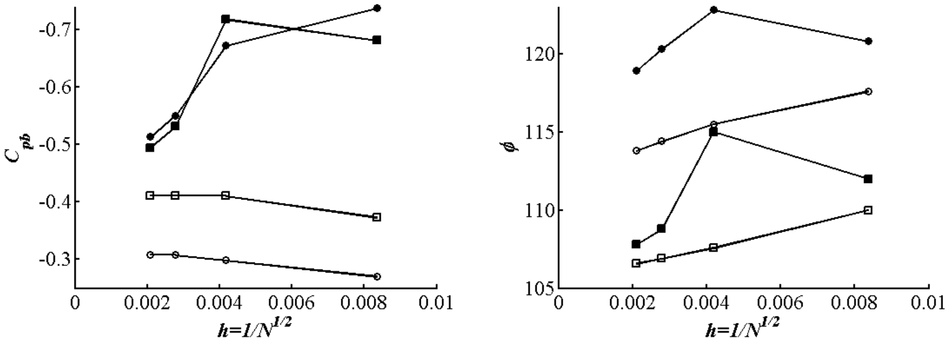

a) **b)**

Figure 7. Results of the grid sensitivity study for a) base pressure coefficient and b) separation angle in a flow around a circular cylinder at $Re = 3.6 \times 10^6$. Notations: — ○ — RANS k-ω model, — ● — URANS k-ω model, — □ — RANS SST model, — ■ — URANS SST model.

Figure 6 represents the transient loads on the cylinder in flow simulations at *Re* = 3.6 × 10^6 with the *k*-*ω* turbulence model corresponding to the initial and boundary conditions specified in section III.B. After roughly $t^* =$ 125, the solution becomes unsteady and oscillations start to occur, therefore causing vortices to shed at a periodic rate. Steady oscillations are observed at $t^* > 400$. Time-averaged statistics are collected during the steady oscillations phase for $t^* = 300$. Figure 8 shows contours of the mean streamwise velocity and the spanwise instantaneous vorticity obtained with the SST turbulence model in the steady oscillation state *Re* = 3.6 × 10^6.

A Fast Fourier Transform (FFT) method is applied to the lift coefficient data to determine the frequency of vortex shedding behind the cylinder. For the considered Reynolds numbers (*Re* = 10^6, 2 × 10^6, 3 × 10^6, 3.6 × 10^6), the computed values of the Strouhal number vary from 0.113 to 0.117, which are rather small to compare with the experimental data. Earlier studies[12-17,31] have found that regular shedding does not occur in the range $10^6 \leq Re \leq 3.5 \times 10^6$. Schewe[14] measured a "jump" in the Strouhal number to roughly 0.4 around $Re = 0.5 \times 10^6$. At the same time, the Strouhal number was measured in Ref. 14 to be 0.1 in the range $0.5 < Re < 2 \times 10^6$. After $Re \approx 2 \times 10^6$, Shih[17] only reported the Strouhal number for rough cylinders, where the Strouhal number increased from 0.2 to 0.25 with increasing Re. The lowest Strouhal number in Ref. 17 corresponds to a cylinder with the most rough surface. Stringer et al.[28] found that OpenFOAM underpredicted the Strouhal number in this flow regime. They recorded *St* to be almost zero and explained it by OpenFOAM's incapability to realistically capture the shedding frequency of the flow in the supercritical regime. Another possible contributing factor to the computed Strouhal numbers being different from those measured in experiments is two-dimensional simulations of three-dimensional flow[21]. One may also postulate that the entire boundary layer is not completely turbulent, therefore requiring a transitional turbulence model to accurately capture the vortex shedding.[18] Additional investigation of this matter is

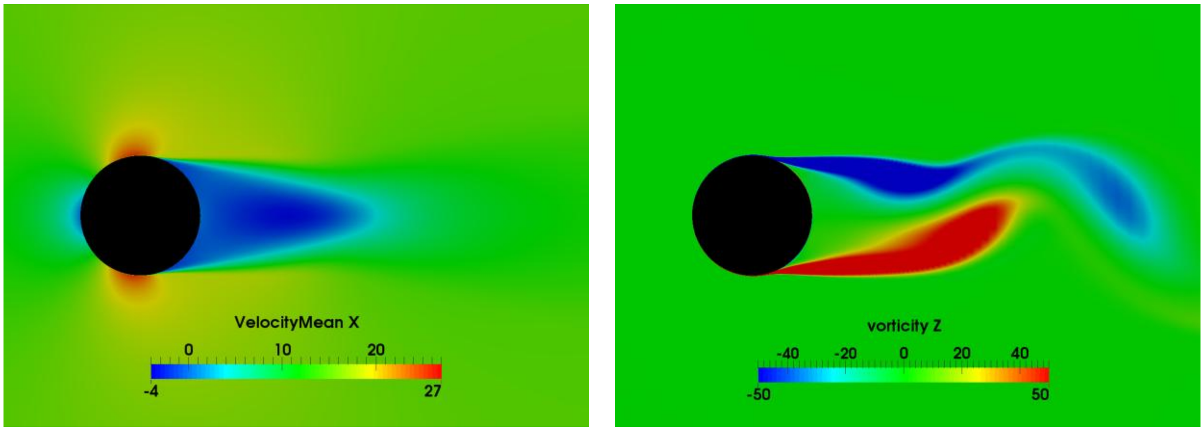

a) **b)**

Figure 8. Cylinder contour plots on the G4 mesh with the SST turbulence model at $Re = 3.6 \times 10^6$. a) mean streamwise velocity, $U_\infty = 14.64\, m/s$ and b) spanwise instantaneous vorticity.

required, but not conducted in the current study due to time constraints.

Computed time-averaged coefficient of drag and base pressure coefficient are within the measured experimental results[12-17] and the wake is clearly turbulent due the delayed separation angle and a narrow wake[18,30] (Table 3 and Fig. 8).

Table 3 compares the drag coefficient, C_D, separation angle, ϕ, recirculation length, L_r/D, and the base pressure coefficient, C_{pb}, at different Reynolds numbers. The recirculation region, L_r/D, in the wake has a large variety of values. The URANS results for the averaged recirculation length are in a better agreement with the reference data, than the RANS results. The bubble length is overpredicted in RANS simulations. At $Re = 10^6$ and 3×10^6, the L_r/D and separation angle, ϕ, produced by the URANS SST turbulence model is close to LES and DES results.[18,21] At $Re = 3.6 \times 10^6$, the L_r/D and ϕ from URANS k-ω turbulence model are close to DES data.[22] In general, the separation angle increases and L_r/D decreases with increasing Reynolds number. The length of the recirculation length is visually represented in Fig. 8a, for the k-ω turbulence model at $Re = 3.6 \times 10^6$.

Table 3 Computed and measured parameters of a flow around a circular cylinder ("~" denotes unavailable data), ("†" denotes Re=3.6×10^6), ("§" denotes rough cylinder).

Turbulence modeling approach	$Re(10)^6$	C_D	St	ϕ	L_r/D	$-C_{pb}$
2D RANS k-ω	1	0.3588	~	108.4°	1.61	0.364
2D URANS k-ω	1	0.4987	0.161	114.1°	0.44	0.625
2D RANS SST	1	0.4808	~	101.3°	1.68	0.448
2D URANS SST	1	0.5070	0.137	102.7°	1.25	0.569
3D RANS k-ε[18]	1	0.39	~	~	~	0.33
3D URANS k-ε[18]	1	0.40	0.31	~	1.37	0.41
3D LES[18]	1	0.31	0.35	103°	1.04	0.32
2D URANS k-ε[19]	1	0.34	0.2	~	~	0.30
2D URANS k-ε[20]	1	0.5174	0.2823	~	~	~
2D RANS k-ω	2	0.3268	~	111.5°	1.47	0.336
2D URANS k-ω	2	0.4467	0.166	116.9°	0.43	0.560
2D RANS SST	2	0.4458	~	104.3°	1.57	0.429
2D URANS SST	2	0.4513	0.113	105.3°	1.32	0.523
2D RANS k-ω	3	0.3100	~	113.1°	1.40	0.317
2D URANS k-ω	3	0.4220	0.170	118.3°	0.42	0.532
2D RANS SST	3	0.4265	~	105.9°	1.51	0.420
2D URANS SST	3	0.4257	0.116	106.8°	1.30	0.495
3D DES/DES with corrections[11]	3	0.41/0.51	0.35/0.33	111°/106°	1.0/1.0	0.53/0.64
2D RANS k-ω	3.6	0.3029	~	113.8°	1.37	0.308
2D URANS k-ω	3.6	0.4107	0.171	118.9°	0.42	0.513
2D RANS SST	3.6	0.4181	~	106.6°	1.49	0.411
2D URANS SST	3.6	0.4206	0.148	107.8°	1.23	0.495
2D URANS k-ε[20]	3.6	0.4703	0.3052	114°	~	~
3D DES/DES with 65° trip[22]	3.6	0.576/0.535	0.305/0.311	118°/119°	0.35/0.32	0.796/0.748
Experimental data						
Roshko[13] §	1-3.5	0.3−0.7	0.27	~	~	0.62-0.85
Schmidt[16]	1-5	0.18−0.53	~	~	~	0.35−0.60
Achenbach[12] §	0.5-5	0.6−0.76	~	115°-120°	~	0.85 †
Jones et al.[15]	0.5-8	0.15−0.54	0.3	~	~	0.53−0.63
Schewe[14]	1-5	0.22−0.52	0.2-0.27	~	~	~
Shih[17]	0.3-8	0.16-0.50	0.2-0.25	~	~	0.10−0.60

Figure 9 is a graphical representation of Table 3 for the time-averaged drag coefficient and the base pressure coefficient. In URANS simulations, the drag coefficient oscillates between maximum and minimum values relating directly to the loads oscillation on the cylinder. The peak coefficient of drag varies between 0.4598 and 0.5332 at $Re = 10^6$ for the k-ω turbulence model and in a range of 0.5054-0.5087 for the SST turbulence model. At $Re = 3.6 \times 10^6$ the peak drag coefficient varies in ranges of 0.3778-0.4387 (Fig.7) and 0.4197-0.4217 for the k-ω and SST turbulence models, respectively.

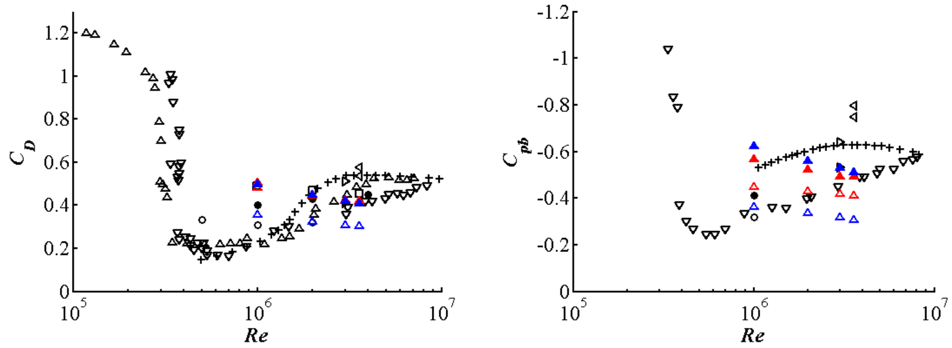

a) b)

Figure 9. Variation of flow parameters with the Reynolds number: a) drag coefficient and b) base pressure coefficient. Computations: △ RANS k-ω (RANS), ▲ URANS k-ω, △ RANS SST, ▲ URANS SST, ○ LES[18], ● URANS[18], □ URANS[20], ▷ DES[21], ◁ DES[22]. Experiments: ▽ Shih[17], △ Schewe[14], + Jones et al.[15]

The drag coefficient values reported in Achenbach[12] and Roshko[13] are significantly higher than those in Schewe,[14] Jones et al.,[15] Schmidt,[16] and Shih.[17] A later study conducted by Roshko[29] found that the cylinders used in earlier experiments[12,13] were rough, thus contributing to overpredicted C_D. These experiments were also conducted in a small wind tunnel with the low aspect ratio using small diameter circular cylinders that affected measured data[30].

At $Re = 10^6$, the separation angle obtained with the URANS SST turbulence model occurs at the same location as reported by Catalano et al.[18] The value of recirculation length from the URANS SST simulations falls between the LES and URANS data reported by Catalano et al.[18] Drag coefficients found in the URANS SST and k-ω simulations are close to the values reported by Ong et al.[20], but differ from the experimental data of Schewe,[14] Jones et al.,[15] Schmidt,[16] and Shih.[17]. Figure 9 confirms that the drag coefficient is overpredicted at $Re = 10^6$ by all models. URANS simulations conducted with the SST and k-ω turbulence models at $Re = 2 \times 10^6$ closely match the available experimental data[15,16] for C_D. Steady-state calculations with the k-ω turbulence model underpredict the C_D values at $Re \geq 2 \times 10^6$, but produce results in agreement with the experimental data in unsteady simulations. There is no significant difference in the C_D values found in steady and unsteady simulations with the SST turbulence model. URANS simulations seem to be preferential for predicting the C_{pb} values at higher Reynolds numbers (Fig. 9b). Steady simulations with the two turbulence models tend to underpredict this parameter. At lower Reynolds numbers, the discrepancy between experimental data is rather large for conclusive statements.

At $Re = 3 \times 10^6$, the values of C_D for URANS simulations with the two turbulence models and for steady RANS SST simulations fall in the same range of values as those produced with DES and obtained in experiments.[14-17,21] This is not the case for other flow parameters, particularly those generated with the URANS k-ω turbulence

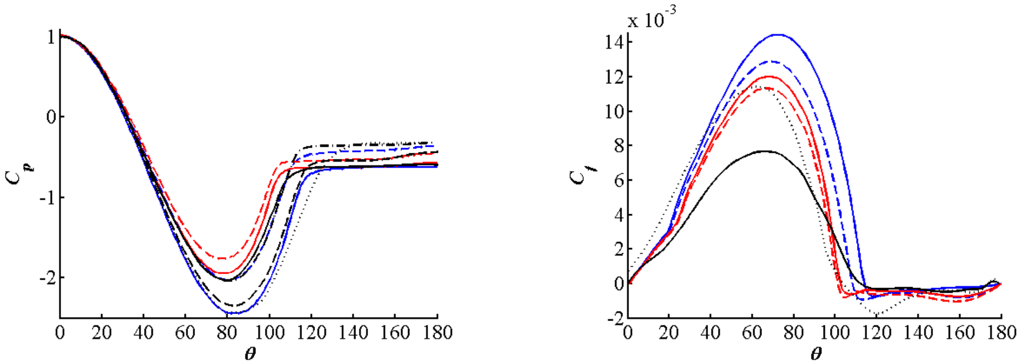

a) b)

Figure 10. Surface parameters with respect to the azimuth angle measured clockwise from the stagnation point at $Re = 10^6$: a) pressure coefficient, b) friction coefficient. Notations: — — RANS k-ω, —— URANS k-ω, — — RANS SST, —— URANS SST, — · — RANS k-ε[18], — — URANS k-ε[18], · · · LES[18], —— URANS k-ε[20].

model. It is interesting to note that this model generates results for the recirculation length and the separation angle in a close agreement with 3D DES[22] at $Re = 3.6 \times 10^6$, but not for other parameters.

Figure 10 shows the surface pressure coefficient, C_p, and the friction coefficient, C_f, $Re = 10^6$. The pressure coefficients calculated with the two turbulence models closely follow computational data from Refs. 18 and 20 on the front side of the cylinder. At about $\theta = 50°$, the difference between all computational data appears and this difference reaches its maximum close to the cylinder top. RANS/URANS SST and RANS k-ω results are close to the RANS k-ε and URANS k-ε data from Refs. 18 and 20, respectively. URANS k-ω results closely follow LES and URANS k-ε data[18,20].

When comparing RANS and URANS simulations, the adverse pressure gradient calculated with the URANS SST model is increased causing the separation angle to increase and providing a more accurate solution. Unsteady simulations with the k-ω turbulence model have the strongest effect on all calculated parameters as shown in Table 3 due to greatly increased the adverse pressure gradient causing the C_p curve to closely match the results from URANS k-ε model and LES data from Ref. 18.

For the friction coefficient at $Re = 10^6$, the difference between the calculated profiles is more pronounced than for the pressure coefficient except within the separation zone. The friction coefficient profile and the separation angle from the simulations conducted with RANS/URANS SST turbulence model are close to those from LES.[18] The large variance in predictions of the friction coefficient with different turbulence modeling approaches explains the difference in reported values of the drag coefficient.

Figure 11 compares pressure and friction coefficients with the DES data.[21] Traven et al.[21] reported that the simulation results were improved with the rotation/curvature term, RC. Therefore, two sets of DES data are available at this Reynolds number. Results obtained with RANS/URANS SST turbulence models closely match the DES data including the prediction of the separated angle $\phi \approx 106°$. The k-ω turbulence model overpredicts values of the two coefficients in comparison with the DES data.

Results for pressure and friction coefficients at $Re = 3.6 \times 10^6$ are shown in Fig. 12. No model provides results for the pressure coefficient consistent with the experimental data at $\theta > 50°$. For the friction coefficient, all models are in a good agreement with the experiment in the separation zone. Predictions of the pressure coefficient conducted with the URANS k-ω model closely follow DES data,[22] whereas results obtained with the URANS SST model are in agreement with the URANS k-ε data.[20] The friction coefficient is overpredicted by both models when compared with the data from Refs. 12 and 20. At $Re = 10^6$, Ref. 20 also has underpredicted C_f when compared to LES data[18] (Fig. 12). This same trend directly applies to a Reynolds number of 3.6×10^6 and explains why C_f is so different. If a linear relationship between the coefficient of friction and Reynolds number is derived from the LES and DES data for $Re = 10^6$ and $Re = 3 \times 10^6$, then our results for $Re = 3.6 \times 10^6$ correlate very well with this relationship. It should be noted that the C_f value from Ref. 12 was measured in a small wind tunnel, on a rough cylinder, and with high blockage, which can explain the significant error between the experimental data and our calculated data. The C_f value at $Re = 3.6 \times 10^6$ is close to DES result[21] conducted at $Re = 3 \times 10^6$ (Fig. 11).

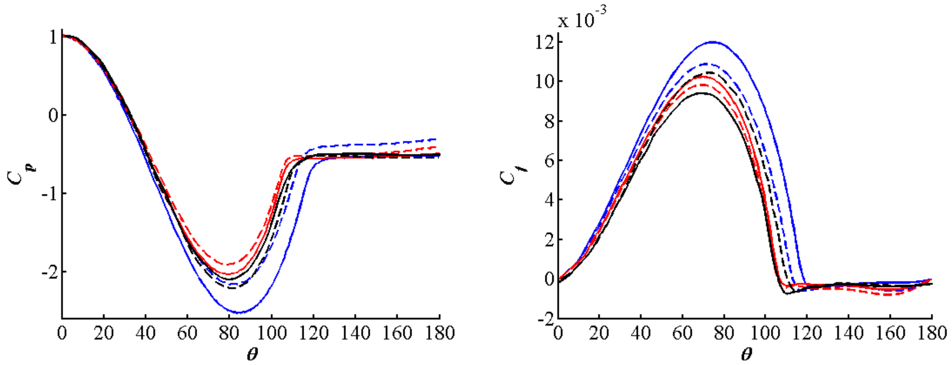

a) **b)**

Figure 11. Surface parameters with respect to the azimuth angle measured clockwise from the stagnation point at $Re = 3 \times 10^6$: a) pressure coefficient, b) friction coefficient. Notations: – – RANS k-ω, — URANS k-ω, – – RANS SST, — URANS SST, – – DES[21], — DES with RC[21].

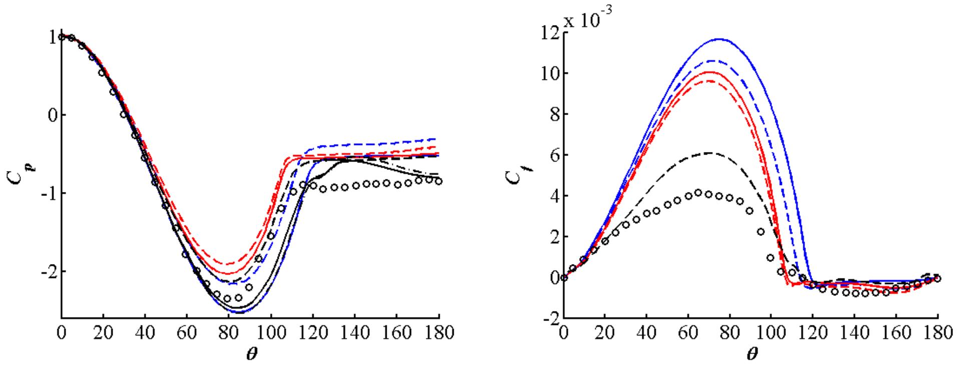

a) b)

Figure 12. Surface parameters with respect to the azimuth angle measured clockwise from the stagnation point at $Re = 3.6 \times 10^6$: a) pressure coefficient, b) friction coefficient. Notations: — — RANS k-ω, —— URANS k-ω, — — RANS SST, —— URANS SST, — — URANS k-ε[20], — · — DES[22], —— DES with 65° trip[22], ○ experimental data[12].

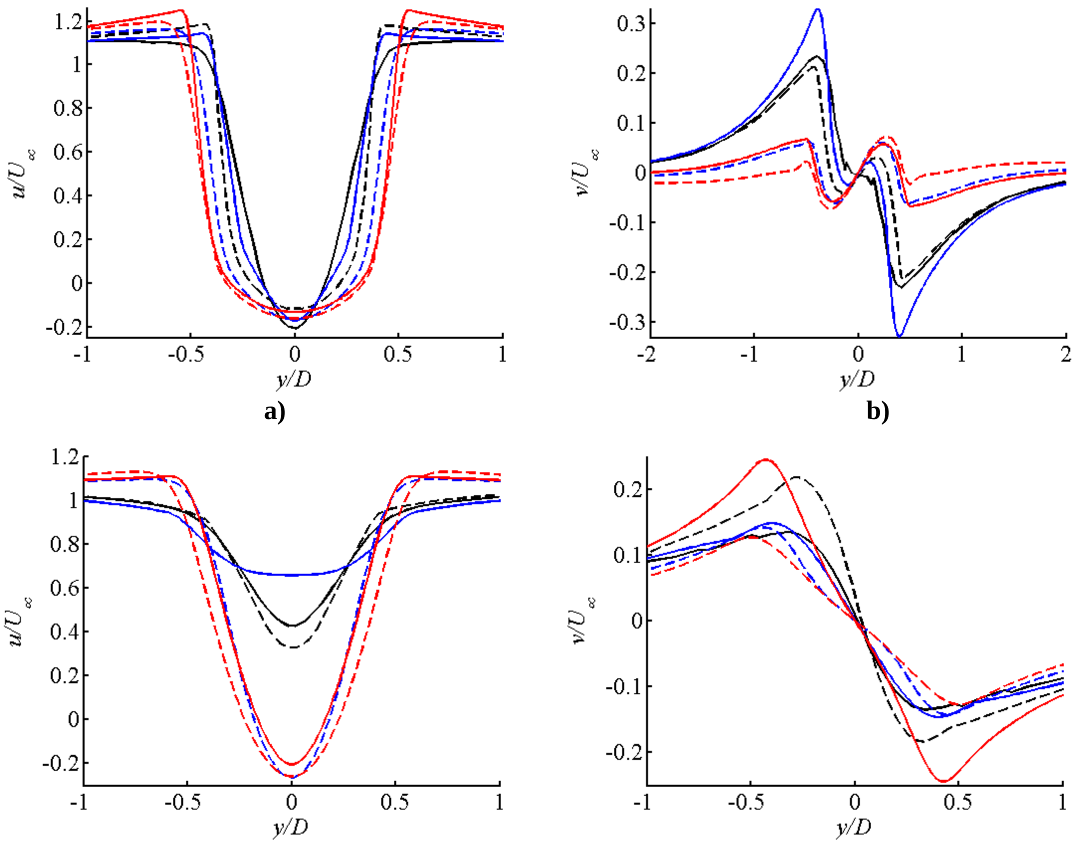

c) d)

Figure 13. Wake results at $Re = 10^6$. a) streamwise velocity component, u/U_∞, at $x/D = 0.75$ b) vertical velocity component, v/U_∞, at $x/D = 0.75$ c) streamwise velocity component, u/U_∞, at $x/D = 1.5$ d) vertical velocity component, v/U_∞, at $x/D = 1.5$. Notations: — — RANS k-ω, —— URANS k-ω, — — RANS SST, —— URANS SST, — — URANS k-ε[18], —— LES[18].

Comparing RANS and URANS results shown in Figures 10b-12b, the C_f values are increased in the adverse pressure gradient zone generated in URANS simulations, with the URANS k-ω turbulence model overpredicting C_f

in all simulations due to the delayed separation angle (Table 3). The most accurate results are produced with the URANS SST model for this parameter.

It is clear from Figures 10-12, that simulation results are less sensitive to a choice of a turbulence model at small and large azimuth angles, that is, in the front part of a cylinder and within the separation zone. The friction coefficient is a more sensitive parameter to predict than the pressure coefficient.

Figure 13 compares velocity profiles calculated with different modeling approaches at $Re = 10^6$. Both steady RANS formulations closely follow the same general trend in the near, $x/D = 0.75$, and far, $x/D = 1.5$, wake. The URANS k-ω turbulence model closely matches LES data[18] in the near wake at $x/D = 0.75$. However, in the far wake at $x/D = 1.5$, the k-ω turbulence model tends to underpredict the maximum value of the streamwise velocity to compare with the results produced with other models. One can postulate that using an unsteady formulation of the k-ω turbulence model enhances the dissipation in the system. Velocity profiles are less affected by changing from steady to unsteady simulations when the SST turbulence model is used.

Conclusions

When unsteady flow simulations were attempted in a flow around the NACA 4412 airfoil, no physically oscillating solution was generated with either of the two turbulence models, SST and k-ω, implemented in OpenFOAM at considered flow parameters. The tendency was observed for unsteady-flow simulations to convert to steady-state formulations regardless of the time step and the accuracy order of time-discretization schemes used.

In a flow around a circular cylinder, unsteady simulations were conducted with both models. The similar trends were observed in all simulations at considered Reynolds numbers with both turbulence models when comparing RANS and URANS result; that is, the surface friction, drag coefficient, and separation angle tend to increase in URANS simulations. Overall, the SST turbulence model captures the flow properties with higher accuracy than the k-ω turbulence model does. The results produced with the k-ω turbulence model are more sensitive whether RANS or URANS formulation is used. Simulation results obtained in the current study are in a qualitative agreement with the results from other computational studies. However, no simulation approach seems to consistently outperform others. More accurate and detailed experimental database would be useful for quantitative comparison of turbulence modeling approaches.

OpenFOAM is a suitable solver for URANS simulations at $Re \geq 2 \times 10^6$ for a smooth circular cylinder, although the shedding frequency predictions are of concern. Additional investigation into this matter is required.

Acknowledgements

The material is in part based upon work supported by NASA under award NNX12AJ61A and by the Junior Faculty UNM-LANL Collaborative Research Grant. A part of the simulations were conducted using the high-performance facilities of the UNM Center for Advanced Research Computing.

References

[1] C. L. Rumsey, T. B. Gatski, W. L. Sellers III, V. N. Vatsa, and S. A. Viken, "Summary of the 2004 CFD Validation Workshop on Synthetic Jets and Turbulent Separation Control," *Proc. the 2nd AIAA Flow Control Conference*, Williamsburg, VA, March 2004.

[2] 11th ERCOFTAC/IAHR Workshop on Refined Turbulence Modelling, April 7-8, 2005, Chalmers Univ. of Technology, Sweden

[3] 12th ERCOFTAC/IAHR/COST Workshop on Refined Turbulence Modelling, October 12-13, 2006, Institute for Fluid Mechanics and Technical Acoustics, Technical University of Berlin, Germany.

[4] M. A. Leschziner, "Modelling turbulent separated flow in the context of aerodynamic applications," *Fluid Dynamics Research*, Vol. 38, No. 02, 2006, pp. 174-210.

[5] J. C. Vassberg, E. N. Tinoco, M. Mani, B. Rider, T. Zickuhr, D. W. Levy, O. P. Brodersen, B. Eisfeld, S. Crippa, R. A. Wahls, J. H. Morrison, D. J. Mavriplis, M. Murayama, "Summary of the Fourth AIAA Computational Fluid Dynamics Drag Prediction Workshop," *Journal of Aircraft*, Vol. 51, No. 04, 2014, pp. 1070-1089.

[6] Menter, F. R., "Two-Equation Eddy-Viscosity Turbulence Models for Engineering Applications," *AIAA Journal*, Vol. 32, No. 8, August 1994, pp. 1598-1605.

[7] Wilcox, D. C., "Formulation of the *k-ω* Turbulence Model Revisited," *AIAA Journal*, Vol. 46, No. 11, 2008, pp. 2823-2838.

[8] Turbulence Model Benchmarking Working Group Turbulence Modeling Resource, NASA Langley. URL: http://turbmodels.larc.nasa.gov/flatplate.html

[9] OpenFOAM, Open-source Field Operation and Manipulation, Software Package, Ver. 2.2.0, 2011. URL: http://www.openfoam.com/

[10] Habbit, III, R. D., Porteous, A. B., Echavarria, C. M. L., Poroseva, S. V., and Murman, S. M., "Computational Analysis of a Flow Around Two-Dimensional Streamlined Bodies with OpenFOAM," AIAA2015-0519, *Proc. AIAA SciTech*, Kissimmee, FL, January 4-8, 2015.

[11] Gomes, S., Graves, B., Poroseva, S. V., "On the Accuracy of RANS Simulations of 2D Boundary Layers with OpenFOAM," AIAA2014-2087, Proc. *the AIAA Aviation and Aeronautics Forum and Exposition*, Atlanta, GA, June 16-20, 2014.

[12] Achenbach, E. "Distribution of Local Pressure and Skin Friction around a Circular Cylinder in Cross-Flow up to Re = 5× 10^6," *Journal of Fluid Mechanics*, Vol. 34, No. 04, 1968, pp. 625-639.

[13] Roshko, A., "Experiments on the Flow Past a Circular Cylinder at Very High Reynolds Number," *Journal of Fluid Mechanics*, Vol. 10, No. 03, 1961, pp. 345-356.

[14] Schewe, G., "On the Force Fluctuations Acting on a Circular Cylinder in Crossflow from Subcritical up to Transcritical Reynolds Numbers," *Journal of fluid mechanics*, Vol. 133, 1983, pp. 265-285.

[15] Jones, G. W., Cincotta, J. J., and Robert, W. W., "Aerodynamic Forces on a Stationary and Oscillating Circular Cylinder at High Reynolds Numbers," *NASA TR R-300*, Washington, D.C., February 1969.

[16] Schmidt, L. V., "Fluctuating Force Measurements Upon a Circular Cylinder at Reynolds Numbers up to 5×10^6," *Meeting on Ground Wind Load Problems in Relation to Launch Vehicles*, Langley Research Center, June 7-8, 1966.

[17] Shih, W. C. L., Wang, C., Coles, D., and Roshko, A., "Experiments on Flow Past Rough Circular Cylinders at Large Reynolds Numbers," *Journal of Wind Engineering and Industrial Aerodynamics*, Vol. 49, No. 1, 1993, pp. 351-368.

[18] Catalano, P., Wang, M., Iaccarino, G., and Moin. P., "Numerical Simulation of the Flow Around a Circular Cylinder at High Reynolds Numbers," *International Journal of Heat and Fluid Flow*, Vol. 24, No. 4, 2003, pp. 463-469.

[19] Karabelas, S. J., Koumroglou, B. C., Argyropoulos, C. D., and Markatos, N. C., "High Reynolds Number Turbulent Flow Past a Rotating Cylinder," *Applied Mathematical Modelling*, Vol. 36, no. 1, 2012, pp. 379-398.

[20] Ong, M. C., Utnes, T., Holmedal, L. E., Myrhaug, D., and Pettersen, B., "Numerical Simulation of Flow Around a Smooth Circular Cylinder at Very High Reynolds Numbers," *Marine Structures*, Vol. 22, No. 2, 2009, pp. 142-153.

[21] Travin, A., Shur, M., Strelets, M., and Spalart, P., "Detached-Eddy Simulations Past a Circular Cylinder," *Flow, Turbulence and Combustion*, Vol. 63, 1999, pp 293-313.

[22] Lo, S.-C., Hoffmann, K. A., and Dietiker, J.-.F., "Numerical Investigation of High Reynolds Number Flows over Square and Circular Cylinders," *Journal of Thermophysics and Heat Transfer*, Vol. 19, No. 1, 2005, pp. 72-80.

[23] Coles, D., and Wadcock, A. J., "Flying-Hot-Wire Study of Flow Past an NACA 4412 Airfoil at Maximum Lift," *AIAA Journal*, Vol. 17, No. 4, April 1979, pp. 321-329

[24] Wadcock, A. J., "Structure of the Turbulent Separated Flow around a Stalled Airfoil," *NASA-CR-152263*, February 1979.

[25] Wadcock, A. J., "Investigation of Low-Speed Turbulent Separated Flow around Airfoils," *NASA Contractor Report No. 177450*, 1987.

[26] Poroseva, S. V., OpenFOAM source files, University of New Mexico. URL:
http://www.unm.edu/~poroseva/researchInterests/

[27] Iaccarino, G., Ooi, A., Durbin, P. A., Behnia, M., "Reynolds Averaged Simulation of Unsteady Separated Flow," *International Journal of Heat and Fluid Flow*, Vol. 24., No. 2, 2003, pp. 147-156.

[28] Stringer, R. M., Zang, J., and Hillis, A. J., "Unsteady RANS Computations of Flow Around a Circular Cylinder for a Wide Range of Reynolds Numbers," *Ocean Engineering*, Vol. 87, 2014, pp. 1-9.

[29] Roshko, A., "On The Aerodynamic Drag of Cylinders at High Reynolds Numbers," *In Proceedings of Seminar on Wind Loads on Structures*, Honolulu, Hawaii, October 19-24, 1970, pp. 87-98.

[30] Zdravkovich, M. M., *Flow Around Circular Cylinders A Comprehensive Guide Through Flow Phenomena, Experiments, Applications, Mathematical Models, and Computer Simulations*, Oxford University Press, 1997.

[31] Schlichting, H., *Boundary Layer Theory, Etc*. (pp. 16-21, 30-33, 40-43), Pergamon Press: London, Verlag G. Braun: Karlsruhe, Karlsruhe Printed, 1955.